Consistency of Viscous Drag Identification Tests for Wave Energy Applications

Giuseppe Giorgi
Centre for Ocean Energy Research, Maynooth University
Co.Kildare, Ireland
E-mail: giuseppe.giorgi.2015@mumail.ie

John V. Ringwood
Centre for Ocean Energy Research, Maynooth University
Co.Kildare, Ireland
E-mail: john.ringwood@nuim.ie

Abstract—**Viscous drag forces in mathematical models for wave energy converters are usually modelled by means of a term based on the Morison equation. Due to large relative velocities, induced by control strategies in order to increase the power absorption, viscous losses can have a high impact on the model accuracy and, in turn, on the model-based power optimization control strategies. Notwithstanding the importance of a reliable estimation of the drag coefficient in the Morison equation, much inconsistency and low trustworthiness is found in the literature, about both the values themselves, and the identification methods.**

Indeed, drag identification for wave energy applications is particularly challenging, mainly due to the device dimensions, characteristic flow regimes, large motions and, in particular, the presence of the free surface. An ideal identification test would be able to replicate the full complexity of the flow, and concurrently to isolate viscous forces from other forces and nonlinear effects. This paper seeks to discuss the inherent challenges to drag identification, proper to wave energy applications. Moreover, different identification techniques are implemented, evaluated and compared, with regard to the estimation of the drag coefficient for a floating heaving point absorber.

Index Terms—**Nonlinear modelling, viscous drag coefficient, Morison equation, computational fluid dynamics, wave energy converters.**

I. Introduction

Accurate modelling of interactions between wave energy converters (WECs) and the surrounding fluid is not trivial, since nonlinear effects, which depend on relative displacement and relative velocity between the device and the water, are likely to be important. Although linear models for WECs are often used, linear assumptions are not fulfilled when large motions occur, which is the necessary condition for a profitable energy generation. Indeed, the objective of maximizing the power extraction is pursued by the control strategy by increasing the amplitude of motion of the device.

Considering heaving point absorbers (HPAs), [1] shows that, without control, the device behaves as a wave follower, with small relative displacement and relative velocity; consequently, nonlinear effects are not excited, and linear models are accurate. In particular, under *uncontrolled* conditions, viscous drag forces are negligible for HPAs [2]. Nevertheless, real wave energy systems always include a control strategy: under *control* conditions, viscous forces become fundamental for HPAs, as shown in [3].

Furthermore, modelling nonlinearities is crucial for the control strategy to achieve maximum power extraction: despite viscous drag introduces losses, the optimal control forces are much more effective if they take into account such losses in the optimization strategy, as shown in [4].

The most common way of including viscous drag effects in mathematical models for WECs is through a Morison-like term [2], based on the Morison equation [5]. The Morison equation was introduced in the 50s, for describing forces on cables of oil platforms and, afterwards, it has been applied in the wave energy field, to describe viscous effects. Despite several decades have passed, there is still some inconsistency in the literature about drag coefficient values for wave energy applications. As an example, drag coefficients for a flap-type device found in the literature vary from 1.9 [6] to 8 [7]. Likewise, the drag coefficient for the Wavestar device [8], which is a piercing heaving sphere, is 0.2 according to [9], 0.5 according to [10], and 1.0 according to [7]. Furthermore, once the drag coefficient is chosen, there is still some uncertainty about the value itself, since often a sensitivity analysis is performed, with variation from zero to twice the value, as in [7].

On top of that, there is no consensus with regard to which drag coefficient estimation technique has to be used. Either the standard literature about viscous drag forces, from outside the wave energy field, is used (constant flow around a fully-submerged body), like in [11], or specific tests are performed, in real or numerical wave tanks. Considering a piercing HPA, [2] carries out harmonic prescribed motion tests with a fully-submerged device. A variation of such an approach is proposed in this paper, with the difference of a saw motion (triangle wave) instead of harmonic. [9] performs radiation experiments instead, so that two fluid phases are considered (water and air), and the free surface is modelled. Finally, as in this paper, the drag coefficient can be identified from the response of the device, subject to incoming waves.

Inaccuracies in the drag coefficient estimation process, for wave energy applications, are due to the flow conditions reproduced in the experiment, which are often not consistent with and/or descriptive of the actual flow around a WEC responding to waves, especially under controlled conditions. Indeed, wave energy applications are particularly challenging due to the characteristic dimensions of the devices, the presence of the free surface (two fluid phases, non-constant wetted surface, radiation and diffraction forces), high displacement

and velocities induced by the control strategy and, overall, a complex flow around the body.

This paper implements and compares five different identification experiments (single phase constant flow, single phase harmonic and saw prescribed motion, radiation tests, and wave response), discussing their appropriateness and applicability in the context of wave energy applications. OpenFOAM [12] is the computational fluid dynamics (CFD) software used for the three-dimensional numerical simulations, to extract the hydrodynamic force acting on the device. The drag coefficient is then evaluated by means of a least-square curve fitting against the Morison equation. The use of CFD, in particular OpenFOAM, has been validated against experimental data, and show to produce accurate results [13], [14].

The remainder of the paper is organized as follows: Sect. II describes the characteristics of the flow around a WEC, focusing on the requirements and challenges for identification experiments. Sect. III describes each identification technique, presenting pros and cons, and results. Finally, Sect. IV presents some final remarks and considerations.

II. Flow Around A Wave Energy Converter

Uncertainties and low trustworthiness of the drag coefficient for WECs are mainly consequences of the complex and challenging fluid flow around a device in its operating conditions. In this paper a piercing HPA is considered as an example, based on the Wavestar device [8]. The geometry is a half submerged sphere of 5 m diameter, and a latching control strategy is implemented.

In general, WECs are large bodies, therefore experimental tests in real wave tanks are usually performed at small scale. An inherent consequence of scaling is the change of flow regime, which is typically laminar at small scale, whereas turbulent at full scale [15]. Such scalability issues may be overcome by using numerical wave tanks in a CFD environment. However, a reliable numerical modelling of turbulence in CFD is a challenging task, requiring time and user experience [16]. Some main issues are discussed in Sect. III-A.

Apart from the geometry, the flow regime around the device is determined by the relative velocity of the fluid with respect to the body. Indeed, a dimensionless number, representative of the flow regime, is the Reynolds (Re) number [17], which is defined, for a fixed body fully-submerged in a fluid with constant velocity v_0, as:

$$Re = \frac{v_0 D}{\nu} \tag{1}$$

where D is the characteristic dimension of the body (the diameter in the case of a sphere), and ν is the kinematic viscosity. However, due to the action of waves, WECs are typically oscillating; therefore, v_0 refers to the maximum relative velocity achieved during the oscillation [17]. An other relevant dimensionless number, used to characterized the flow around oscillating bodies, is the Keulegan-Carpenter KC number [17], defined for fixed fully-submerged bodies in harmonic flow, as:
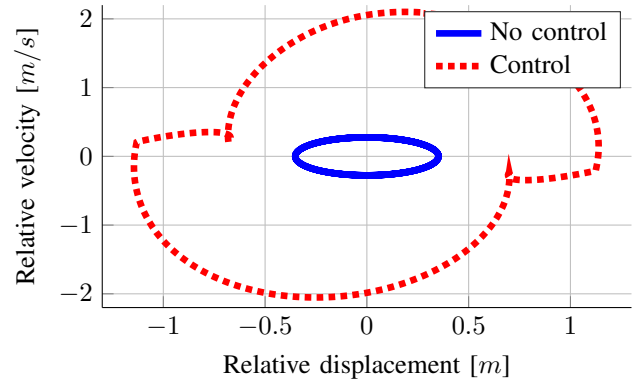

Fig. 1. Operational space for the heaving point absorber, subject to a regular wave condition (wave period $T_w = 8s$, wave height $H_w = 1m$), under uncontrolled (PTO acting as a simple damper), and controlled (latching control) conditions.

$$KC = \frac{2\pi A_0}{D} \tag{2}$$

where A_0 is the amplitude of motion of the fluid particles.

An effective identification experiment should reproduce Re and KC numbers consistent to the flow around a WEC, in its operating conditions. In particular, it is important to consider the response of the device under controlled conditions, since the operational space of relative amplitude and relative velocity is considerably enlarged: Fig. 1 shows an example of operational space, computed in CFD, for the HPA subject to a regular wave condition.

The response of the HPA, under controlled conditions, is studied for a set of regular wave conditions, with wave period T_w ranging from 5s to 10s, and wave height H_w ranging from 0.5m to 2m. The resulting KC numbers are found between 0.56 and 3.11, while Re numbers are between 3.56e6 and 1.79e7. Since the laminar-turbulent transition of a sphere is at a Re of about 1e6 [16], the resulting flow is highly turbulent.

Nevertheless, note that the definition of Re and KC numbers, as well as the standard viscous drag theory (outside the wave energy field), refers to fully-submerged bodies. On the contrary, (floating) wave energy applications have to deal with the presence of two fluid phases (water and air), and the dynamical changes of the free surface elevation, making Re and KC numbers less representative of the resulting complex flow regime.

When a piercing device is considered, the wetted surface of the body is continuously changing, so does the magnitude of the hydrodynamic force, including the viscous drag force. Furthermore, forces related to the deformation of the free surface elevation come into play, namely radiation and diffraction forces. Highly nonlinear effects may arise, especially when the controller induces large amplitudes of motion, including air bubbles trapped in the fluid close to the surface of the body, splashes, and water jets. Fig. 2 shows how the latching control strategy causes large variations of the wetted surface of a heaving sphere.

(a) Top position without control.

(b) Bottom position without control.

(c) Top position with control at the unlatching instant.

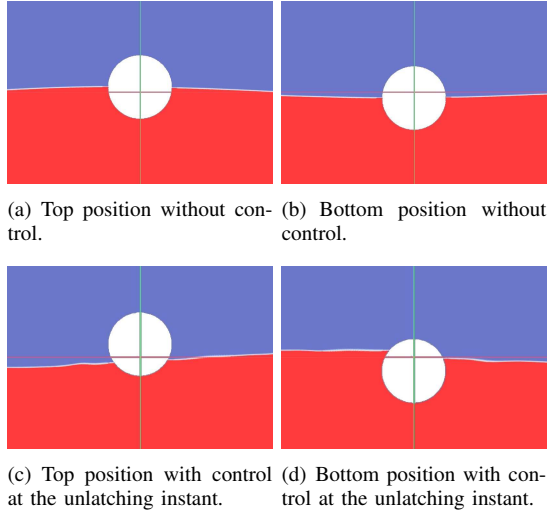(d) Bottom position with control at the unlatching instant.

Fig. 2. Screen-shots of CFD simulations with and without control applied [3]. The red region on the bottom represents water, whereas the blue on the top represents air.

An ideal drag identification test would be able to replicate the full complexity of the flow around the device, and concurrently isolate viscous forces. Unavoidably, as the flow complexity increases, more nonlinear effects and interactions occur, making the isolation of the viscous drag force more challenging. Several different identification tests exist which, based on different choices and assumptions, give up some fidelity of the flow replication, in order to gain an easier isolation of the drag force. Five different drag coefficient identification techniques are described and compared in Sect. III.

III. IDENTIFICATION TECHNIQUES

The dynamics of a heaving floating WEC can be described, in the linear potential theory framework [18], by the Newton's second law:

$$m\ddot{\mathbf{z}} = \mathbf{F}_{FK_{st}} + \mathbf{F}_{FK_{dy}} + \mathbf{F}_D + \mathbf{F}_R + \mathbf{F}_{PTO} + \mathbf{F}_{vis} \quad (3)$$

where m is the mass of the device, $\mathbf{z}$ the vertical displacement, $\mathbf{F}_{FK_{st}}$ the static Froude-Krylov (FK) force, $\mathbf{F}_{FK_{dy}}$ the dynamic FK force, $\mathbf{F}_D$ the diffraction force, $\mathbf{F}_R$ the radiation force, $\mathbf{F}_{PTO}$ the power take-off (PTO) force, and $\mathbf{F}_{vis}$ the viscous drag force. Note that, according to linear potential theory, it is assumed that amplitudes of motion and wave steepness are small, implying the superposition principle valid.

Usually, $\mathbf{F}_{vis}$ is based on the Morison equation [5], which was introduced in the '50s to describe wave forces on cables of offshore structures, and is used to model the total force acting on fixed small bodies, compared to the wave length:

$$\mathbf{F}_{Mor} = -\frac{1}{2}\rho \, C_d A_d \, |\mathbf{V}_0| \, \mathbf{V}_0 - \rho \, (1 + C_m) V_d \dot{\mathbf{V}}_0, \quad (4)$$

where ρ is the fluid density, C_d is the drag coefficient, C_m is the inertia coefficient, A_d is the characteristic area, $\mathbf{V}_0$ is

the undisturbed flow velocity, and V_d the volume of displaced fluid.

Consequently, the literature outside the wave energy field, concerning the Morison equation, often refers to cylindrical (cable-like) small bodies, with the consequent Re and KC numbers. Conversely, in wave energy applications, only the velocity term of equation (4) is used to describe viscous effects acting on large bodies, considering the relative velocity between the velocity of the floater $\mathbf{V}$ and the undisturbed flow velocity [2]:

$$\mathbf{F}_{vis} = -\frac{1}{2}\rho \, C_d A_d \, |\mathbf{V} - \mathbf{V}_0| \, (\mathbf{V} - \mathbf{V}_0), \quad (5)$$

Note that the characteristic area is the projection of the instantaneous wetted surface onto a plane normal to the flow. Since, equation (5) is proportional to C_d, and to the relative velocity squared, the viscous force is more sensitive to changes of velocities, rather than C_d. Therefore, even though C_d typically decreases with larger velocity [17], the overall viscous force increases.

In order to identify the drag coefficient C_d in (5), specific experiments are performed, in real or numerical wave tanks, and the total force acting on the body is measured. Then, $\mathbf{F}_{vis}$ is isolated from other (eventually present) forces, and C_d is estimated as the one which minimizes the error between the measure and the model, using, for example, a least square approach, as shown in [2].

Experiments are designed in order to replicate (to some extent) the flow surrounding the device, in its operating conditions, and concurrently allow isolating the viscous drag force from forces of other nature. Major flow characteristics, discriminating between different estimation techniques, regard the number of fluid phases (one —fully-submerged body—, or two —floating body—), the relative flow (constant, harmonic, saw), and the body motion (fixed, prescribed, dynamic response). Finally, it is important to use the identification tools with large displacements and velocities (KC and Re), appropriate to wave energy applications, which may be different from other field applications.

In this paper, the drag coefficient is identified for a floating heaving sphere, with latching control. The following approaches are considered and compared:

(A) Fully-submerged, fixed body, constant flow: see Sect. III-A

(B) Fully-submerged, prescribed motion, harmonic flow: see Sect. III-B

(C) Fully-submerged, prescribed motion, saw flow: see Sect. III-C

(D) Floating, prescribed motion, harmonic flow (radiation test): see Sect. III-D

(E) Floating, dynamic response: see Sect. III-E

The geometry studied is a 5m diameter sphere which, when the free surface is modelled (approaches (D) and (E)), has its centre at the still water level. Fig. 2 shows a cross-section of the three-dimensional CFD simulations of the sphere, subject to incoming wave (approach E). CFD simulations,

for approaches (A) to (D), have been performed using 24 cores, each one carrying a processor Intel (R) Xeon (R) CPU E5-2440 0 @ 2.40GHz. Simulations for the approach (E) where more computationally demanding; therefore, they have been performed on a high-performance computing cluster, made available by the Irish Centre for High-End Computing (ICHEC) [19].

A. Fully-submerged, fixed body, constant flow

The established viscous drag theory refers to bodies immersed in a single fluid (usually air or water), subject to constant unidirectional flow. The Re number is defined for such flow conditions, and it determines the passage from laminar to turbulent flow, which happens at a Re number around 1e6 for a sphere. One main phenomenon involved in the viscous drag force is the point of flow detachment, which moves upstream around the surface of the sphere, as the Re number increases [16].

A constant flow around a fixed body is a complex, but well-known process, and a conspicuous amount of literature deals with experimental tests or CFD numerical simulations. Achieving accurate results with CFD numerical tools requires time and user experience, but main guidelines are available in the literature [20]. In particular, accurately estimating hydrodynamic forces at high Re numbers requires an appropriate description of turbulences and vortexes close to the surface of the body. An important role is played by the flow solver: large eddy simulation (LES) solvers should be preferred to Reynolds averaged simulation (RAS) solvers, since they are able to solve turbulent flows more accurately.

Another crucial parameter is the thickness of the boundary layer, namely the distance of the first mesh cell from the body surface. The quality of the boundary layer mesh is evaluated by means of a dimensionless parameter, called y^+, which should be between 40 and 200, when wall functions are used [20]. The y^+ number is defined as follows:

$$y^+ = \sqrt{\frac{\tau_w}{\rho}} \frac{y}{\nu} \qquad (6)$$

where τ_w is the wall shear stress, and y the distance to the nearest wall. In general, the mesh discretization should always be evaluated through convergence studies.

Note that, such guidelines are less representative for oscillatory flows and/or two fluid phases, so more care must be used in the simulation set up. Indeed, with oscillatory flows, the fluid velocity is reversing, so the flow is never steady, and y^+ values are constantly changing. Furthermore, the Re number is less representative of the flow regime, because reversing velocities may cause the creation of further vortices, even at Re lower than 1e6 [17]. Moreover, the point of flow detachment moves back and forth around the sphere surface, as the velocity changes magnitude and direction. Finally, the eventual presence of two fluid phases makes the notion of flow detachment more blurred.

Despite such major differences in the flow characteristics, having only a constant unidirectional flow around a fixed body

provides a perfect isolation of the drag force term, which is indeed the only force acting on the body, since accelerations and free surface forces are absent. However, the drag coefficient must be evaluated at very high Re numbers (up to about 2e7), which are required by wave energy applications, as discussed in Sect. II. Identifying a value for C_d in such very turbulent conditions is not straightforward, due to vortex induced vibrations [21], which cause high-frequency forced oscillations. Fig. 3 shows, indeed, the drag force in laminar and turbulent conditions, at Re of 1e5 and 1e7, respectively. In the CFD simulations, initial conditions consider a constant flow velocity throughout the fluid domain. The same constant velocity is imposed on the inlet and outlet boundaries, while the lateral boundaries have a slip velocity condition. The slow transient in Fig. 3 depends on the perturbation that the velocity field undergoes, due to the presence of the body, and the drag coefficient (in laminar flow) can be identified by the steady state force. As a matter of fact, the data in the literature usually refer to experiments for Re numbers up to 2e6, just above the laminar-turbulent transition limit.

$$v_0 = 0.02 m/s, Re = 1e5$$

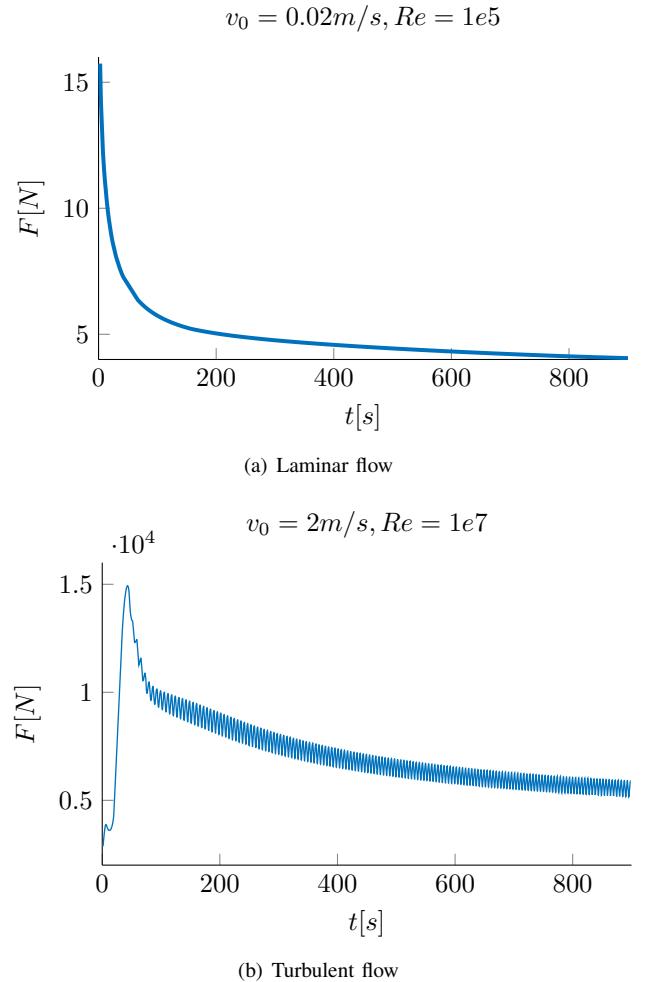(a) Laminar flow

$$v_0 = 2 m/s, Re = 1e7$$

(b) Turbulent flow

Fig. 3. Fluid force on a fixed sphere, 5m diameter, fully-submerged in a flow with constant velocity v_0.

TABLE I
HARMONIC PRESCRIBED MOTION AMPLITUDES AND PERIODS, FOR A
FULLY-SUBMERGED SPHERE (5 M DIAMETER) IN CALM WATER, AND
RESULTING REYNOLDS AND KEULEGAN-CARPENTER NUMBERS.

Re		$A[m]$			
		0.5	1	1.5	2
	3	5.24E+06	1.05E+07	1.57E+07	2.09E+07
$T[s]$	6	2.62E+06	5.24E+06	7.85E+06	1.05E+07
	9	1.75E+06	3.49E+06	5.24E+06	6.98E+06
	12	1.31E+06	2.62E+06	3.93E+06	5.24E+06
KC		0.63	1.26	1.88	2.51

TABLE II
ESTIMATED DRAG COEFFICIENTS, USING HARMONIC PRESCRIBED MOTION
FOR A FULLY-SUBMERGED SPHERE IN CALM WATER, WITH RESPECT TO
THE CASE STUDY TABULATED IN TABLE I.

C_d		$A[m]$			
		0.5	1	1.5	2
	3	0.29	0.19	0.15	0.10
$T[s]$	6	0.27	0.17	0.14	0.14
	9	0.29	0.18	0.15	0.14
	12	0.31	0.20	0.16	0.15

TABLE III
ESTIMATED DRAG COEFFICIENTS, USING SAW PRESCRIBED MOTION FOR A
FULLY-SUBMERGED SPHERE IN CALM WATER, WITH RESPECT TO THE
CASE STUDY TABULATED IN TABLE I.

C_d		$A[m]$			
		0.5	1	1.5	2
	3	0.06	0.05	0.05	0.04
$T[s]$	6	0.09	0.06	0.06	0.05
	9	0.12	0.08	0.07	0.06
	12	0.14	0.09	0.08	0.07

B. Fully-submerged, prescribed motion, harmonic flow

The device is fully immersed in calm water, and it is driven to follow a harmonic trajectory, so that the relative flow between the fluid and the body is known. Due to the absence of the free surface, the only hydrodynamic forces acting on the surface depend on the acceleration and velocity; therefore, the two coefficients of the Morison equation (4) are identified, namely C_d and C_m.

Compared with the constant flow approach, discussed in Sect. III-B, while the oscillatory (rather than constant) flow is more representative of the intended WEC application, the presence of two force components (rather than one) makes the identification of the drag coefficient more challenging. Indeed, it results that the inertial term of equation (4) is predominant, making the total force less sensitive to the velocity term. As a consequence, small variations of the total force, due to the CFD numerical set up, cause significant variations in the drag coefficient identification. In such a context, convergence studies are particularly relevant. The background mesh has been selected iteratively, in order to achieve y+ values within the range [40, 200], as suggested in [18]. Furthermore, the convergence of the amplitude of the total hydrodynamic force acting on the device has been checked. The same method has been applied for all identification approaches. The final computational time of each CFD simulation, for approach (B) is about 300 times larger than the simulation time.

A fully-submerged sphere (5 m diameter) is studied, forced to follow a set of 16 harmonic trajectories, with 4 equispaced periods T, from 3s to 12s, and 4 equispaced displacement amplitudes A, from 0.5m to 2m. The resulting Re and KC numbers are tabulated in Table I. The most extreme condition (T of 3s, A of 2m), with the largest velocity, Re and KC numbers, is inspired by the operational conditions of a floating sphere, under latching control conditions: the maximum relative displacement between the free surface elevation and the body is equal to the radius of the device (2.5m); furthermore, as a result of the latching control strategy, the device is let free to move from a peak to a trough, or vice versa, in a period of time similar to the natural period of the device (about 3.2s) [22].

The prescribed motion (position, velocity and acceleration) of the body is harmonic, and the resulting force acting on the body is proportional to the acceleration and the velocity squared, consistent with (4), since the velocity of the still water

is zero. Following a least square approach, C_m and C_d are identified such as the error between the force measured in CFD and the Morison force, in (4), is minimized. While C_m is significantly constant, equal to 0.5, large variations are found for C_d, whose values are tabulated in Table II.

C. Fully-submerged, prescribed motion, saw flow

On the one hand, experiments with constant flow, discussed in Sect. III-A, have the advantage of having only the velocity term of the Morison equation, but at the price of unidirectional flow. On the other hand, (bidirectional) harmonic prescribed motion experiments, discussed in Sect. III-B, have the advantage of modelling a more representative oscillatory flow, but with the drawback of having both the acceleration and velocity terms of the Morison equation to identify.

A novel identification test is herein proposed, in the attempt of reproducing only the advantages of the two previous methods, without the related disadvantages. A triangle wave (or saw) motion is imposed on the device, so that the flow is bidirectional while maintaining a constant velocity (apart from the edges of the saw, where the velocity changes sign). The same case study as in Sect. III-B, tabulated in Table I, is considered. The resulting drag coefficients are tabulated in III.

Comparing the results using harmonic and saw prescribed motions, in Table II and III, respectively, one can notice the same overall trend is followed, with larger drag coefficients at smaller Re numbers. On the other hand, drag coefficients identified using saw motion experiments are smaller.

D. Floating, prescribed motion, harmonic flow

A further degree of complexity is added to the identification experiment, with the objective of a more accurate reproduction of the flow conditions around the operating WEC. In particular, vertical harmonic prescribed motions are imposed on a floating body in calm water. Notwithstanding the advantage of a having an experimental set up more similar to the intended WEC

TABLE IV
ESTIMATED DRAG COEFFICIENTS, USING HARMONIC PRESCRIBED MOTION FOR A FLOATING SPHERE IN CALM WATER, WITH RESPECT TO THE CASE STUDY TABULATED IN TABLE I.

C_d		$A[m]$			
		0.5	1	1.5	2
$T[s]$	3	0.35	0.24	0.15	0.06
	6	0.44	0.41	0.34	0.32
	9	0.98	0.69	0.45	0.41
	12	1.19	1.01	0.65	0.46

TABLE V
ESTIMATED DRAG COEFFICIENTS, USING THE DYNAMICAL RESPONSE TO REGULAR WAVES OF A FLOATING SPHERE, UNDER LATCHING CONTROL CONDITIONS.

C_d		$H[m]$			
		0.5	1	1.5	2
$T[s]$	5	0.05	0.05	0.33	0.47
	6	0.06	0.13	0.18	0.19
	7	0.29	0.46	0.49	0.33
	8	0.97	0.81	0.66	0.54
	9	0.88	0.89	0.73	0.59
	10	1.34	1.43	1.15	0.79

application, modelling the free surface introduces other forces (radiation and restoring), and nonlinear effects, as described in Sect. II, making the isolation and identification of the viscous drag force more challenging. Furthermore, the the CFD computational domain must include numerical beaches in order to absorb radiated waves. Consequently, the computational time of each CFD simulation is about 900 times larger than the simulation time, which is 3 times longer than the time required for approaches (B) and (C).

While the radiation force for heaving point absorbers can be assumed to be linear [18], the restoring force presents relevant nonlinearities, due to the non-constant cross sectional area of the sphere. The nonlinear restoring force is computed as the balance between the weight of the device and the integral of the static pressure over the instantaneous wetted surface [23]. Equation (3) is therefore used to compute the total force, which is compared with the measurement from CFD simulations. The same case study as in Sect. III-B, tabulated in Table I, is considered. The resulting drag coefficients are tabulated in IV.

Despite a significant variability, higher estimations of the drag coefficients are overall obtained, in comparison with the results in Tables II and III. Such differences are justified by the influence of other forces and nonlinear effects, introduced by the free surface. Estimations of C_d are particularly sensitive to modelling errors of the restoring force, which is the largest hydrodynamic force, several times larger than radiation and viscous forces [24].

E. Floating, dynamic response

Finally, the dynamic response of the floating device to incoming waves, using a latching control strategy, is considered. On the one hand, the advantage is that none of the characteristics of the flow around a controlled WEC, discussed in Sect. II, is neglected. On the other hand, dealing with the full complexity of such a flow makes the isolation of the viscous drag force impossible. Indeed, several different forces are contributing to the motion of the device, as shown in equation (3), which are likely to be nonlinear, due to large motions, induced by the control strategy.

As a result, the estimated drag coefficient, which minimizes the error between the mathematical model and CFD measurements, is actually a descriptor of all the unmodeled effects/nonlinearities, as well as modelling errors and inaccuracies, as supposed to a descriptor of the drag force only. Therefore, such a drag coefficient may be misleading

and inappropriate if used to evaluate viscous effects only. Nevertheless, if the objective is to fill the gap between the mathematical model and CFD, regardless of the nature or source of the difference, the information incorporated in the drag coefficient can be used effectively to reduce modelling errors, and increase the accuracy of the results. The notion of *equivalent* drag coefficient is introduced, which highlights the fact that nonlinearities, other than viscous drag, may be included in the coefficient itself. Similarly, [25], [26] include all nonlinear viscous effects present in the CFD simulation into a representative *linear* damping term identified from a free decay experiment [25] or adaptively during WEC operation [26].

Nonlinear static and dynamic FK forces are included [23], while radiation and diffraction forces are considered linear, since the wave length is much longer than the diameter of the floating buoy [18]. A set of regular wave conditions are taken into account, with 6 equispaced wave periods T_w, from 5s to 10s, and 4 equispaced wave heights H_w, from 0.5m to 2m. A zero-threshold latching control strategy is implemented [27]. KC (between 0.56 and 3.11), and Re (between 3.56e6 and 1.79e7) numbers are evaluated according to relative displacement and velocity, respectively, obtained in CFD simulations. All the details of the numerical set-up and the computational time require by the CFD simulations are given in [3].

While, according to the prescribed motion approaches (B) to (D), drag coefficients are identified using force signals, the *equivalent* drag coefficient is here evaluated by means of the motion responses instead. The value of C_d is identified such to minimize the least square error between the vertical displacement computed in CFD, and the one computed using the equation of motion (3). The resulting drag coefficients, tabulated in Table V, are significantly varying for different wave conditions, and spread over a wider range of values than the ones obtained with fully-submerged harmonic and saw prescribed motion experiments, tabulated in Tables II and III, respectively. On the other hand, a similar range of values is obtained with the floating harmonic prescribed motion test, tabulated in Table IV. Therefore, it can be implied that free surface-related nonlinearities are affecting the identification of the drag coefficient.

With such a variability of the equivalent drag coefficient for different wave conditions, sensitivity analysis are important to
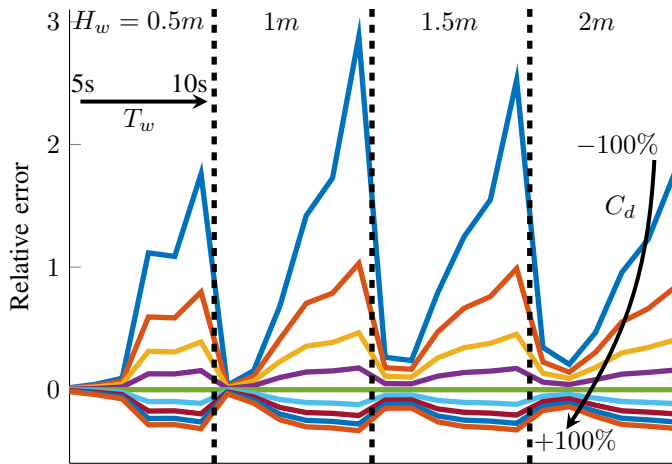
Fig. 4. Sensitivity analysis on the relative error on the power prediction, varying the drag coefficient from -100% to $+100\%$ of the optimal value at each wave condition. Four section are highlighted, for the four wave heights. In each section, the wave period is increasing from left to right.
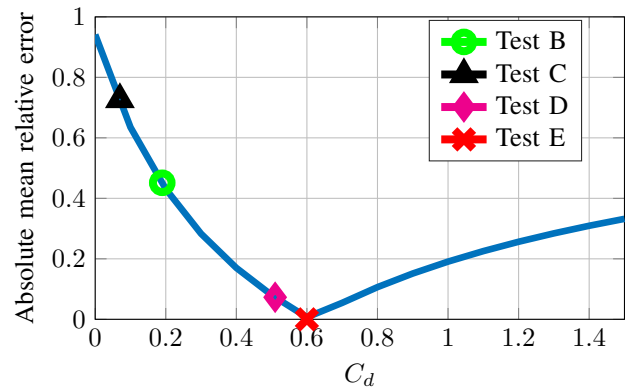

Fig. 5. Absolute mean relative error for a constant drag coefficient across all the considered wave conditions. The markers refers to the mean values identified according to different approaches, as discussed in the respective sections.

TABLE VI
ABSOLUTE MEAN RELATIVE ERROR FOR THE MEAN DRAG COEFFICIENT,
IDENTIFIED ACCORDING DIFFERENT TESTS.

	C_d	Absolute mean relative error
No drag	0	94.1%
Sect. III-B	0.19	45.1%
Sect. III-C	0.07	72.6%
Sect. III-D	0.51	7.3%
Sect. III-E	0.60	0%

evaluate the impact of the viscous drag term and, in particular, of errors in the choice of C_d. For each of the optimal drag coefficient in Table V, nine equispaced relative variations are applied, from -100% to $+100\%$, so from zero to twice the value. The relative error on the power production estimation is used as a sensitivity index, considering, for each wave condition, the model using the optimal drag coefficient as a benchmark. Results are shown in Fig. 4, where positive relative errors stand for power overestimation. Four section are highlighted, for the four wave heights, and in each section, the wave period is increasing from left to right.

Clearly, as C_d increases, larger power losses cause the estimated produced power to decrease. Overall, relative errors are increasing with the wave period, being relatively small for short waves, no matter the value of the drag coefficient, indicating little relevance of viscous forces for wave conditions with low energy content (which cause smaller motion and less nonlinearities).

Furthermore, neglecting viscous forces (first curve from top, in Fig. 4) causes significant errors, and steep improvements are achieved already with a drag coefficient four times smaller than the optimal one (second curve, in Fig. 4). In general, overestimating the drag coefficient is preferable to underestimating it, since the curves at negative relative errors are much closer to zero than the positive curves.

Despite the importance of studying the variations of the drag coefficient for different wave conditions, finally one single value has to be chosen, since WECs operate in more realistic irregular sea states. Therefore, a single constant value is used for all the considered wave conditions, and the mean relative error on the power estimation prediction is computed. The drag coefficient which minimizes the absolute value of the mean relative error across all the wave conditions is selected, equal to 0.6, as shown in Fig. 5. Moreover, it can be seen that the steepness of the curve decreases as C_d increases, confirming

that overestimation of the drag coefficient is to be preferred.

As a comparison, the average drag coefficients according to each one of the other identification tests, Tabulated in Tables II to IV, are shown in Fig. 5, and summarized in Table VI. Note that they are smaller than the optimal one and, in particular, the drag coefficient increases as the flow becomes more complex: the smallest C_d (0.07) is found with the saw motion, which has only a constant velocity. The fully-submerged harmonic motion (velocity and acceleration terms to be identified) returns an average C_d of 0.19. Finally, the radiation test, which includes velocity, acceleration, and free surface effects, gives an average C_d of 0.51. Therefore, it can be speculated that the more complex the flow, the larger the dissipations (due to both viscous drag and other nonlinear effects), the larger the equivalent drag coefficient.

IV. CONCLUSION

Controlled wave energy devices are likely to show nonlinear behaviour, especially due to the large motions induced by the control strategy, in order to increase the power absorption. Therefore, appropriate modelling of nonlinearities, as viscous drag losses, is crucial for the model accuracy, as well as effectiveness of the control strategy. However, due to the high complexity of the flow around WECs (with large oscillating motion in a multiphase fluid field), the estimation of the drag coefficient of the device is challenging, causing uncertainties and inconsistency in literature material.

Drag identification tests must define a proper compromise between pertinence of the flow reproduction, and simplicity

of isolation of the drag term. Pros and cons of five different identification approaches are discussed in this paper, comparing their performance with respect to a floating heaving point absorber, under latching control conditions. In general, it is shown that defining a single representative and comprehensive drag coefficient is a difficult task, due to a large variability of the results, both within and across the different approaches.

On the one hand, the wide range of relative velocities and displacement, experienced by a WEC in its operating (controlled) conditions, causes actual variations of the drag coefficient. On the other hand, as the flow becomes more complex, different sources of nonlinearities, as well as modelling errors, may interfere with the isolation of the viscous drag force, affecting the identification, and causing "apparent" variations of the drag coefficient. As a result, an *equivalent* drag coefficient is identified instead, which incorporates effects other than pure viscous drag. Nevertheless, rather than identifying viscous drag forces, the actual final objective, usually, is to fill the accuracy gap between mathematical models and CFD simulations, for which such an *equivalent* drag coefficient seems to be more effective.

Finally, in spite of large variations of the drag coefficient, it is shown that, even with a non-optimal drag coefficient, errors are drastically reduced if a viscous drag term is included in the mathematical model. Furthermore, in case of uncertainty, sensitivity studies show that it is preferable to choose a larger rather than smaller drag coefficient, since overestimations cause lower errors than underestimations.

REFERENCES

[1] G. Giorgi, M. Penalba, and J. V. Ringwood, "Nonlinear hydrodynamic models for heaving buoy wave energy converters," in *Proceedings of the 3rd Asian Wave and Tidal Energy Conference*, 24-28 October 2016, pp. 144–153.

[2] M. A. Bhinder, A. Babarit, L. Gentaz, and P. Ferrant, "Assessment of viscous damping via 3d-cfd modelling of a floating wave energy device," in *Proceedings of the 9th European Wave and Tidal Energy Conference, Southampton, UK*, 2011.

[3] G. Giorgi and J. V. Ringwood, "Froude-krylov and viscous drag representations in nonlinear wave energy devices models in the computation/fidelity continuum," *Ocean Engineering*, 2017.

[4] G. Bacelli, R. Genest, and J. V. Ringwood, "Nonlinear control of flap-type wave energy converter with a non-ideal power take-off system," *Annual Reviews in Control*, vol. 40, pp. 116–126, 2015.

[5] Morison, J.R., M., Johnson, J.W., Schaaf, and S.A., "The force exerted by surface waves on piles," *Journal of Petroleum Technology*, vol. 2, no. 5, pp. 149–154, May 1950.

[6] M. A. Bhinder, A. Babarit, L. Gentaz, and P. Ferrant, "Effect of viscous forces on the performance of a surging wave energy converter," in *Proceedings of the 22nd International and Polar Engineering Conference, Rhodes, Grece*, June 17-22 2012, pp. 545–549.

[7] A. Babarit, J. Hals, M. Muliawan, A. Kurniawan, T. Moan, and J. Krokstad, "Numerical benchmarking study of a selection of wave energy converters," *Renewable Energy*, vol. 41, pp. 44–63, 2012.

[8] Wavestar, "Wavestar a/s, available at http://wavestarenergy.com/," 2016.

[9] A. S. Zurkinden, F. Ferri, S. Beatty, J. P. Kofoed, and M. Kramer, "Nonlinear numerical modeling and experimental testing of a point absorber wave energy converter," *Ocean Engineering*, vol. 78, pp. 11–21, 2014.

[10] M. M. Jakobsen, "Wave-structure interactions on point absorbers - an experimental study," Ph.D. dissertation, Aalborg University, 2015.

[11] P. M. Schmitt, "Investigation of the near flow field of bottom hinged flap type wave energy converters," Ph.D. dissertation, Queen's University Belfast, 2014.

[12] OpenFOAM, *OpenFOAM The Open Source CFD Toolbox User Guide Version 3.0.1*, 13th December 2015.

[13] A. Iturrioz, R. Guanche, J. Lara, C. Vidal, and I. Losada, "Validation of openfoam for oscillating water column three-dimensional modeling," *Ocean Engineering*, vol. 107, pp. 222–236, 2015.

[14] P. Schmitt and B. Elsaesser, "On the use of openfoam to model oscillating wave surge converters," *Ocean Engineering*, vol. 108, pp. 98–104, 2015.

[15] V. Heller, "Scale effects in physical hydraulic engineering models," *Journal of Hydraulic Research*, vol. 49, no. 3, pp. 293–306, 2011.

[16] A. Ooi, "Openfoam validation for high reynolds number flows," University of Melbourne, Tech. Rep., October 2012.

[17] B. Molin, *Hydrodynamique des structures offshore*. Editions Technip, 2002.

[18] J. Falnes, *Ocean Waves and Oscillating Systems*, C. UK, Ed. Cambridge University Press, 2002.

[19] ICHEC, "Irish Centre for High-End Computing (ICHEC)," 2016. [Online]. Available: https://www.ichec.ie/

[20] J. H. Ferziger, M. Peric, and A. Leonard, "Computational methods for fluid dynamics," 1997.

[21] B. R. Munson, D. F. Young, and T. H. Okiishi, *Fundamentals of fluid mechanics*. John Wiley & Sons, 1990.

[22] G. Giorgi and J. V. Ringwood, "Implementation of latching control in a numerical wave tank with regular waves," *Journal of Ocean Engineering and Marine Energy*, vol. 2, no. 2, pp. 211–226, 2016.

[23] ——, "Computationally efficient nonlinear froude–krylov force calculations for heaving axisymmetric wave energy point absorbers," *Journal of Ocean Engineering and Marine Energy*, pp. 1–13, 2016.

[24] G. Giorgi, M. Penalba, and J. V. Ringwood, "Nonlinear hydrodynamic force relevance for different wave energy converter types," in *Proceedings of the 3rd Asian Wave and Tidal Energy Conference*, 24-28 October 2016, pp. 154–162.

[25] J. Davidson, S. Giorgi, and J. V. Ringwood, "Linear parametric hydrodynamic models for ocean wave energy converters identified from numerical wave tank experiments," *Ocean Engineering*, vol. 103, pp. 31–39, 2015.

[26] J. Davidson, R. Genest, and J. V. Ringwood, "Adaptive control of a wave energy converter simulated in a numerical wave tank," in *12th European Wave and Tidal Energy Conference (EWTEC), Cork*, 2017.

[27] A. Falcao, "Phase control through load control of oscillating-body wave energy converters with hydraulic pto system," *Ocean Engineering*, vol. 35, no. 3, pp. 358–366, 2008.